Journal of Organometallic Chemistry 887 (2019) 86–97

Contents lists available at ScienceDirect

Journal of Organometallic Chemistry

journal homepage: www.elsevier.com/locate/jorganchem

Ultrafast electron-transfer in a fully conjugated coumarin-ferrocene donor-acceptor dyads

Alex J. King [a], Yuriy V. Zatsikha [b], Tanner Blessener [b], Forrest Dalbec [a], Philip C. Goff [c], Mathew Kayser [a, 1], David A. Blank [c, ***], Yuriy P. Kovtun [d, **], Victor N. Nemykin [a, b, *]

[a] Department of Chemistry & Biochemistry, University of Minnesota Duluth, Duluth, MN, 55812, USA
[b] Department of Chemistry, University of Manitoba, Winnipeg, MB R3T 2N2, Canada
[c] Department of Chemistry, University of Minnesota, Minneapolis, MN, 55455, USA
[d] Institute of Organic Chemistry National Academy of Sciences, Kyiv, 02660, Ukraine

ARTICLE INFO

Article history:
Received 8 October 2018
Received in revised form
24 January 2019
Accepted 4 March 2019
Available online 9 March 2019

Keywords:
Coumarin
Ferrocene
Transient absorption spectroscopy
Density functional theory

ABSTRACT

A series of a fully conjugated ferrocene-containing coumarins and B,O-chelated coumarins was prepared and characterized by a variety of spectroscopic (UV–vis, NMR, and mass spectrometry), electrochemical (CV and DPV) and spectroelectrochemical methods. The photophysical properties of the target compounds were investigated by steady-state fluorescence and ultrafast transient absorption spectroscopy methods. Selective photoexcitation of the coumarin core was followed by ultrafast electron transfer from the ferrocene fragment, resulting in formation of a charge-separated Fc^{+}-coumarin$^{-\cdot}$ state. This charge-separated state undergoes ultrafast ground state recovery in 20–25 ps, shortening the excited state lifetime of the organic coumarin precursors (1.2–1.5 ns) by almost two orders of magnitude. Formation of the charge-separated states was supported by the experimental (steady-state fluorescence oxidative titrations) and theoretical DFT and TDDFT calculations.

1. Introduction

Coumarin dyes are frequently employed as fluorescent biomarkers due to high fluorescence quantum yields, and optical stability and tunability [1–3]. The coumarin core is readily amenable to functionalization, leading to an array of specifically tuned bright fluorophores that are soluble in organic solvents and water as well as sensitive to the pH and redox environments [4–7]. Functionalization of the 4-hydroxycoumarin core with the variety of acyl groups at the third position leads to formation of the HO–C=C–C=O fragment, which resembles a chelating β-diketone functional group [8–11]. Metal complexation to these coumarin-based platforms was explored during the last several decades [12–16]. Interaction of the boron trifluoride with β-diketones leads to formation of BF_2 complexes, first reported in 1984 [17]. However, such boron difluoride complexes have not been prepared for the coumarin chromophore until recently [18–24]. During the previous decade, it has been shown that the introduction of conjugated ferrocene group(s) into organic chromophores such as porphyrins [25–28], BODIPYs [29–35], aza-BODIPYs [36,37], and BOPHYs [38,39] results in substantial quenching of the fluorescence that, in some cases, can be partially restored under oxidative conditions. These compounds have received attention as prospective redox-switchable platforms for a range of imaging applications. Although several ferrocene-coumarin dyads have been reported in the literature [40–48], to the best of our knowledge, 4-hydroxycoumarin-based systems with full conjugation between the coumarin core and ferrocene fragments have yet to be reported. In this paper, we discuss preparation and characterization of the ferrocene-coumarin and BF_2-chelated ferrocene-coumarin donor-acceptor dyads **2** and **5** in which the ferrocene group is conjugated to the coumarin core (Scheme 1).

2. Results and discussion

Target ferrocene-containing compounds **2** and **5** were prepared as shown in Scheme 1. First, the condensation reaction between

* Corresponding author. Department of Chemistry & Biochemistry, University of Minnesota Duluth, Duluth, MN, 55812, USA.
** Corresponding author.
*** Corresponding author.
E-mail addresses: blank@umn.edu (D.A. Blank), kovtun@ioch.kiev.ua (Y.P. Kovtun), Viktor.Nemykin@umanitoba.ca (V.N. Nemykin).
[1] Mathew Kayser deceased in August of 2016.

https://doi.org/10.1016/j.jorganchem.2019.03.004
0022-328X/

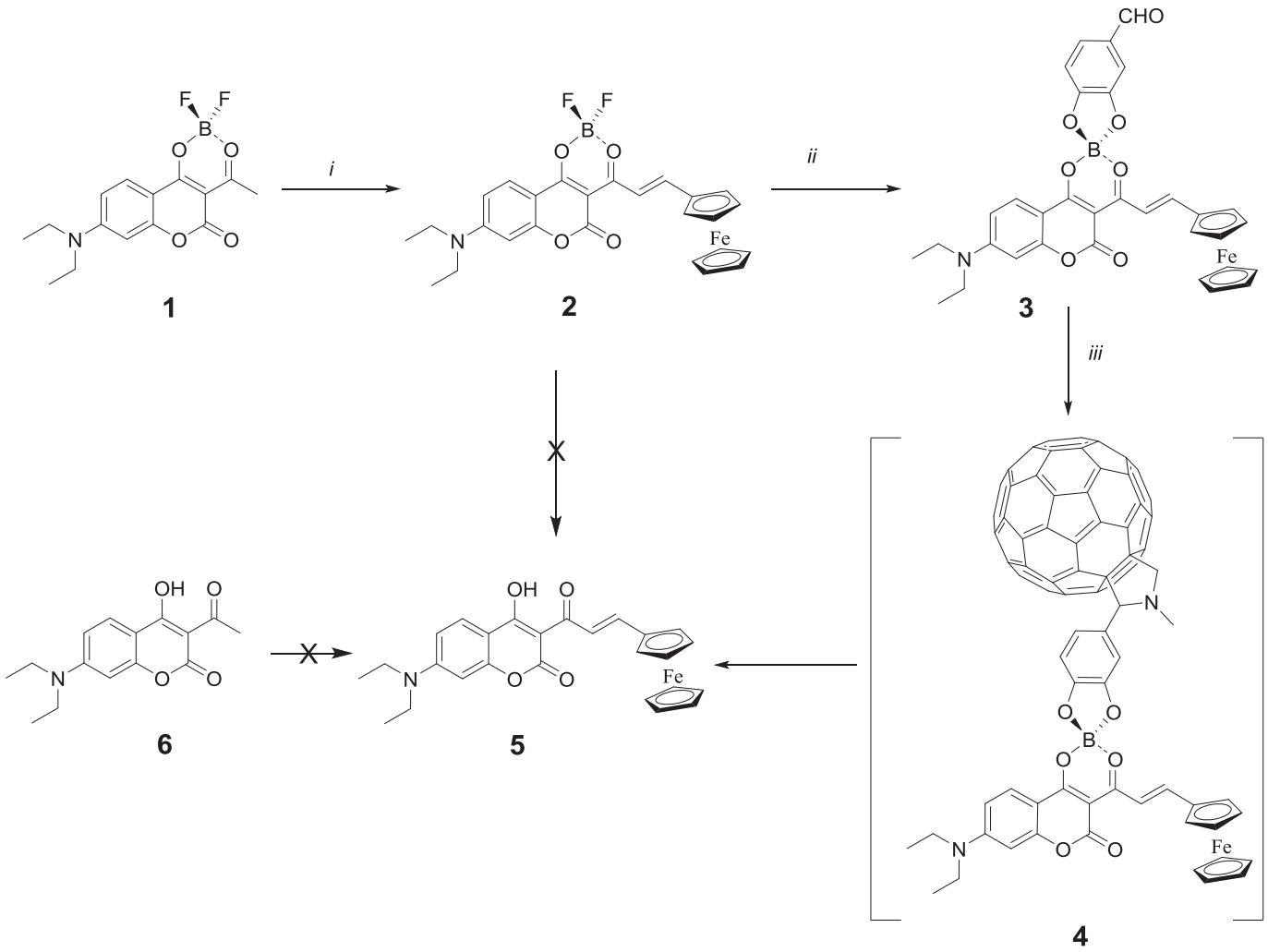

Scheme 1. Synthesis of the target ferrocene-coumarin dyads **2** and **5**.

parent coumarin **1** and ferrocenecarboxaldehyde exploits the acidity of the protons on the acetyl group of **1**, and results in formation of ferrocene-coumarin **2** (Scheme 1). Ferrocene-coumarin **2** can be reacted with 3,4-dihydroxybenzaldehyde, which results in the formation of aldehyde **3**. This aldehyde was thought to be reactive under Prato reaction conditions [49,50] to form ferrocene-coumarin-fullerene triad **4** (Scheme 1). However, the Prato reaction with aldehyde **3** results in formation of unexpected ferrocene-coumarin **5**, which is not accessible from ferrocene-coumarin **2** or parent coumarin **6**.

Structures of all ferrocene-coumarin compounds were confirmed by the standard spectroscopic methods such as NMR and high-resolution mass spectrometry (Supporting Information Figures S1–S8). UV–vis spectra of ferrocene-coumarins **2** and **5** are shown in Fig. 1 along with the spectra of corresponding parent coumarins **1** and **6**, while the numerical values for the molar extinction coefficients are listed in the Experimental Section. In the case of parent compounds **1** and **6**, UV–vis spectra are dominated by a single intense band observed at 389 (**6**) and 428 (**1**) nm, which can be tentatively assigned to the lowest energy $\pi-\pi^*$ transition of coumarin core. Similar to the previous report [24], the shift of ~30 nm to lower energy of the most intense transition in **1** when compared to **6** can be associated with the formation of BF_2-chelated fragment. Presence of the extended π-system in ferrocene-containing **2** and **5,** compared to the parent **1** and **6,** results in

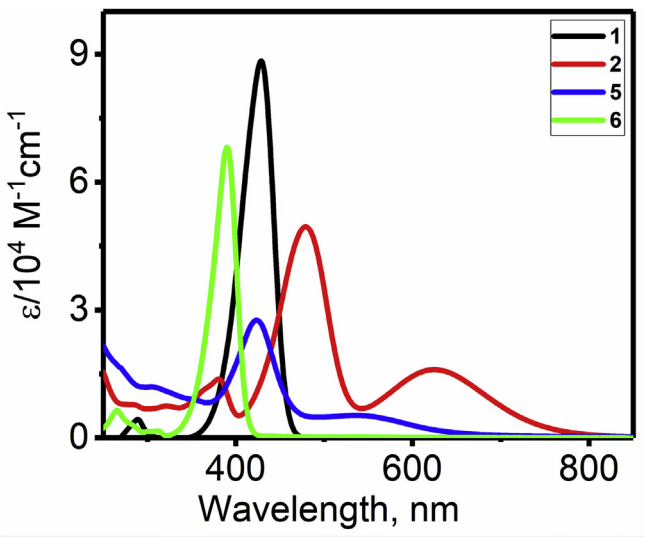

Fig. 1. UV–vis absorption spectra of coumarins **1**, **2**, **5**, and **6** in DCM.

the low-energy shift of the coumarin-centered transition observed at 479 (**2**) and 420 (**5**) nm. In addition, a new, broad band at 541 and 626 nm was observed in the UV–vis spectra of **2** and **5**, respectively (Fig. 1). Based on the similarity of the UV–vis absorption spectra for **2** and **5** with those reported for ferrocene-containing Fc-CH=CH-BODIPY dyads [32], the broad, lower intensity bands observed for dyads **2** and **5** were tentatively assigned to the metal(Fe)-to-ligand(coumarin) charge-transfer (MLCT) transition.

Since the hydroxy groups in compounds **5** and **6** could be deprotonated at high pH, and the protonation of the diethylamino group in **1**, **2**, **5**, and **6** can disrupt conjugation of this substituent with the coumarin core, we conducted UV–vis pH titrations of all target molecules to elucidate the influence of the protonation or deprotonation on their optical properties. When parent coumarin **6** was deprotonated using NBu_4OH as the base to form [**6-H**]$^-$, its most intense $\pi \rightarrow \pi^*$ transition at 389 nm was replaced with a higher-energy band at 333 nm that had ~50% of the original intensity (Fig. 2). Deprotonation of the ferrocene-containing coumarin **5** resulted in disappearance of the MLCT band at 541 nm and $\pi \rightarrow \pi^*$ transition at 420 nm, and the appearance of a higher-energy band at 359 nm (Fig. 2). In contrast, titrations of the BF_2-containing coumarins **1** and **2** with NBu_4OH as the base resulted in only minor reductions in intensity of all major absorption bands. This was attributed to slow hydrolysis of the BF_2 group.

Protonation of the parent coumarins **1** and **6** with a strong acid led to the similar transformation of their UV–vis spectra (Fig. 2). In both cases, the intense $\pi \rightarrow \pi^*$ transition observed at 389 and 429 nm for **6** and **1**, respectively, was replaced with a series of a low-intensity, higher-energy bands. Such a shift to higher energy is expected, as the protonation of diethylamino group in **1** and **6** removes conjugation of the nitrogen atom lone-pair with the coumarin core. A similar higher-energy shift of the most intense $\pi \rightarrow \pi^*$ transition upon protonation was also observed in the ferrocene-containing coumarines **2** and **5** (Fig. 2). However, for both compounds, the intensity of the low-energy MLCT transition was decreased and formation of lower- and higher-energy bands adjacent to the MLCT transition was observed. As shown below, in conjunction with the spectroelectrochemical and TDDFT data, transformation of the UV–vis spectra of **2** and **5** upon protonation can only be explained by simultaneous protonation of the diethylamino group and oxidation of ferrocene fragment by oxygen, which is similar to the oxidation of the parent ferrocene by oxygen in acidic media [51,52].

Redox properties of coumarins **1**, **2**, **5**, and **6** were investigated by cyclic voltammetry (CV) and differential pulse voltammetry

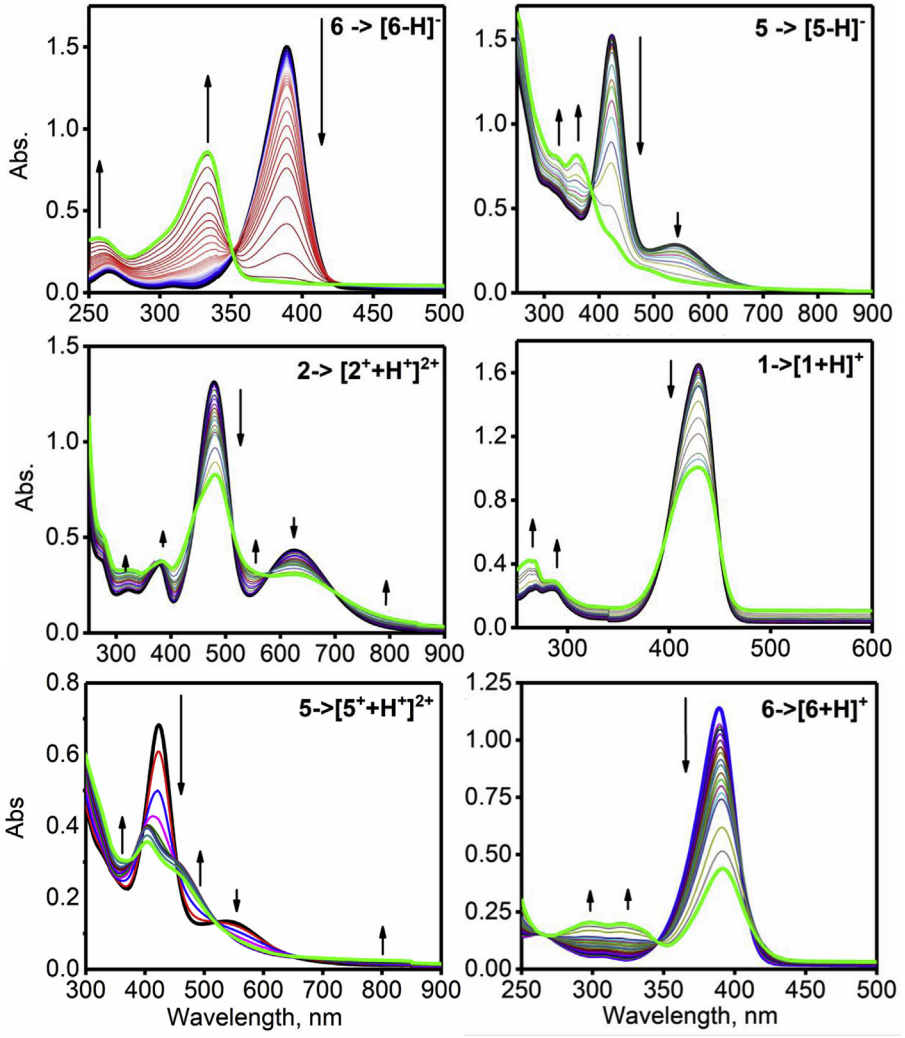

Fig. 2. UV–vis titrations of coumarins **2** and **5** with NBu_4OH in MeOH (top) and UV–vis spectra changes upon titration of coumarins **1**, **2**, **5**, and **6** with trifluoroacetic acid in DCM (middle and bottom).

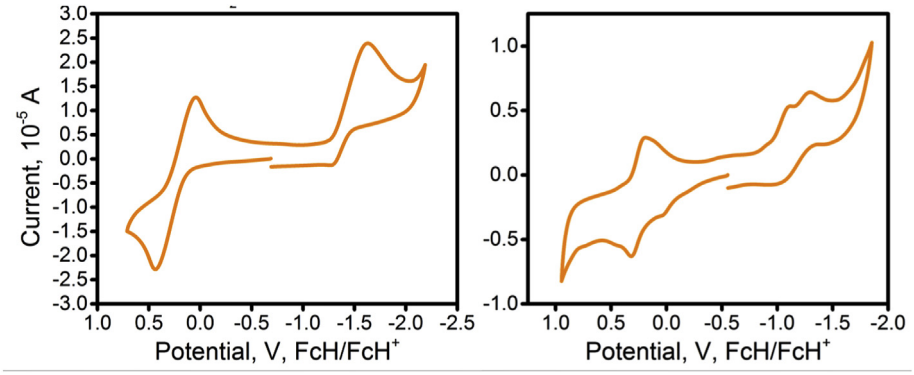

Fig. 3. Electrochemical (CV) data for ferrocene-containing coumarins **2** and **5** in DCM/0.1M TBAP system.

(DPV) (Fig. 3 and Table S1). In the case of parent coumarins **1** and **6,** one irreversible oxidation process was observed along with one (**1**) or two (**6**) irreversible reductions. In the case of ferrocene-containing systems **2** and **5**, one reversible oxidation process was observed in the range typical for ferrocene group oxidation [53]. No coumarin oxidation was observed in **2** or **5**, while reduction processes similar to parent compounds **1** and **6**, respectively, were observed.

Spectroelectrochemical oxidation of the ferrocene-containing coumarins **2** and **5** reveal similar spectroscopic signatures (Fig. 4). In particular, upon oxidation of these compounds, the most intense coumarin-centered $\pi-\pi^*$ transitions at 479 (**2**) and 420 nm (**5**) get reduced in intensity with a higher energy band observed at 362 (**2**) and 359 (**5**) nm appearing in the spectra. The MLCT band at 626 (**2**) and 541 nm (**5**) was reduced in intensity and shifted to higher-energy. These changes are typical for ferrocene-chromophore dyads with ferrocene groups conjugated into the chromophore π-system and are indicative of ferrocene group oxidation. It should be noted, however, that the final spectra of $[\mathbf{2}]^+$ and $[\mathbf{5}]^+$ are different from the UV–vis spectra observed upon protonation of **2** and **5** by trifluoroacetic acid (Fig. 2).

Similar to the other coumarins, parent compound **1** is highly fluorescent [24,54,55]. The steady-state fluorescence is quenched in the ferrocene-containing systems **2** and **5**. Oxidation of the ferrocene-coumarin dyad **2** by $Fe(ClO_4)_3$ in THF results in a partial restoration of the fluorescence in this compound (Fig. 5), which is suggesting that static quenching in **2** and **5** occurred because of the typical electron-transfer process from the ferrocene donor to the photoexcited coumarin acceptor core [32]. Transient absorption spectra of the target coumarins are shown in Fig. 6. In the case of organic chromophores **1** and **6**, the transient absorption spectra

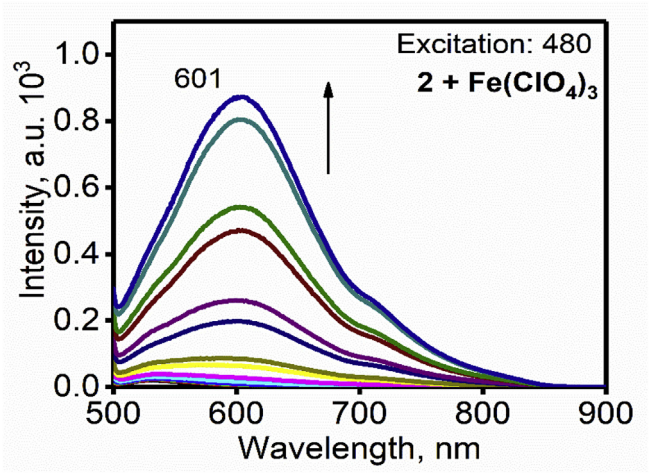

Fig. 5. Partial fluorescence recovery upon oxidation of ferrocene coumarin **2** with $Fe(ClO_4)_3$ in DCM/MeOH mixture.

reflect relaxation of the optically excited state with lifetimes of 1.50 ± 0.02 4, lines and 1.3 ± 0.1 ns respectively (data shown in Fig. S9), typical for a slightly fluorescent (because of the presence of diethylamino group) coumarin derivatives. Pump probe spectra for **2** and **5** are presented in Fig. 6. They both have absorption features on the long wavelength side of the ground state bleach that are not present in the parent compounds. These features are indicative of formation of an Fc^+-coumarin$^{-\cdot}$ charge-separated state, originating from the ultrafast (<200 fs) photo-induced electron-transfer from the ferrocene donor fragment to the coumarin acceptor core. Fig. 6

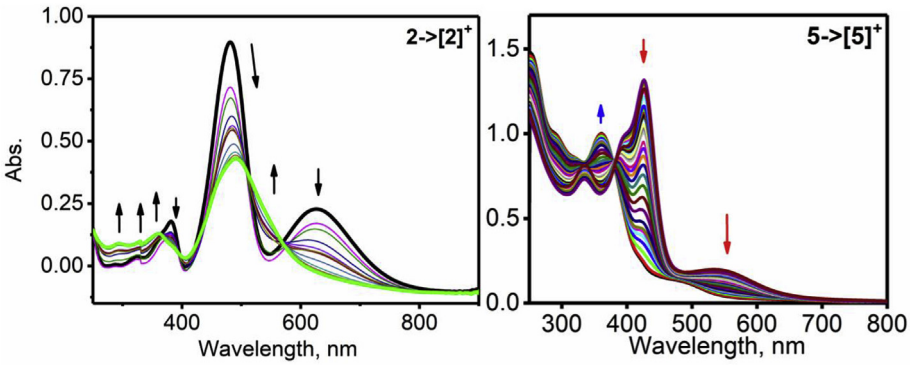

Fig. 4. Oxidation of the ferrocene-containing coumarins **2** and **5** under spectroelectrochemical conditions in DCM/0.3 TBAP system.

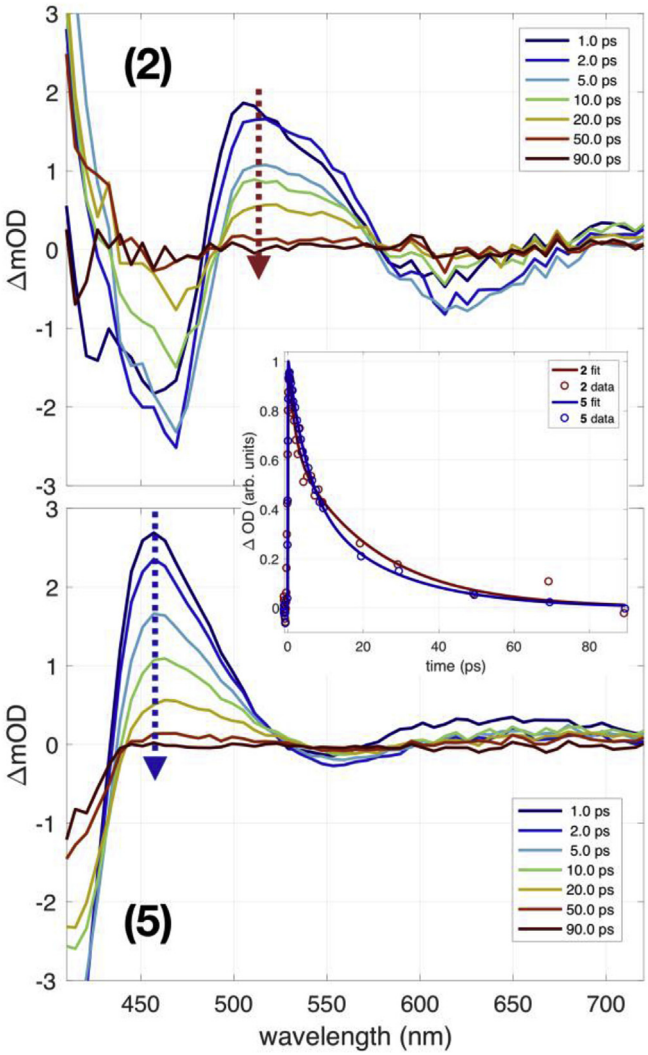

Fig. 6. Pump probe spectra for **2** and **5** in toluene following excitation at 405 nm. The inset shows time evolution of the transient absorption features at the wavelengths indicated by the dashed arrows in the main figure.

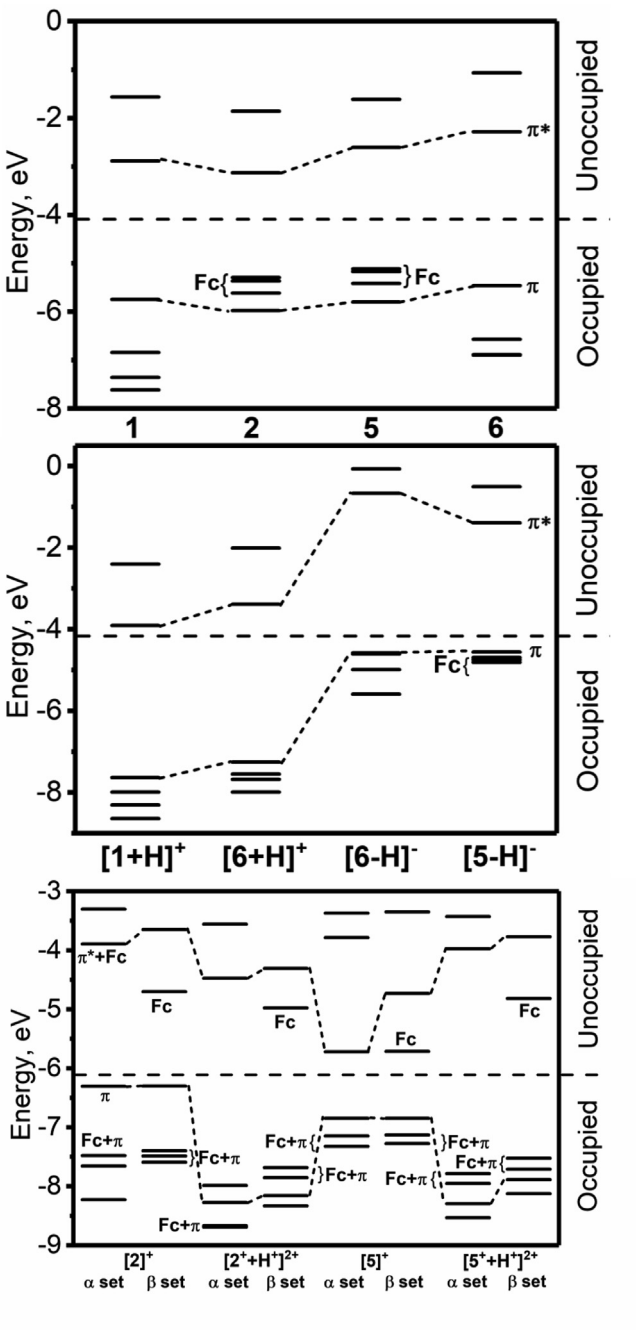

Fig. 7. DFT predicted energy diagram for the target coumarines.

inset presents decay of the transient absorption features at 520 nm (**2**) and 460 nm (**5**). Each of the decays were well fitted by a sum of two exponential decays, and the resulting optimized time constants are presented in Table S2. The shorter time constant in the decay, 1–5 ps, is assigned to reorganization of the charge transfer state and solvent. The longer time constant, 22 ± 4 ps (**2**) and 23 ± 3 ps (**5**), returns the transient absorption to the baseline. This is assigned to decay of the charge-separated state back to the ground state of the complex. We note that this recombination of the charge separated state is ~5 times faster than the analogous ferrocene-BODIPY systems [32].

To provide additional support for the spectroscopic and electrochemical assignments for the target coumarins **1**, **2**, **5**, and **6**, we have conducted Density Functional Theory (DFT) and time-dependent DFT (TDDFT) calculations. The DFT-predicted energy level diagram (Fig. 7), frontier orbitals (Fig. 8) and orbital compositions (Table 1) correlate well with the experimental redox and photophysical properties. In particular, the DFT-predicted HOMO in **1** and **6** consists of nearly identical contributions from the coumarin π-system and the conjugated diethylamino group. The DFT-predicted LUMO in **1** and **6** has only a ~10% contribution from the diethylamino group and is dominated by the coumarin π-system. In contrast, the HOMO in **2** and **5** is dominated by the ferrocene with the LUMO being coumarin-centered. Such electronic structure agrees well with the ferrocene-centered first oxidation process observed in **2** and **5** and opens a pathway for the low-energy MLCT transition in these compounds.

TDDFT calculations are indicative of the presence of the low-energy MLCT bands in **2** and **5,** which have lower energies and oscillator strengths than the coumarin-centered, $\pi-\pi^*$ transitions, while the UV–vis spectra of the parent systems **1** and **6** can be accounted for by the coumarin-centered $\pi-\pi^*$ transitions alone (Fig. 9). TDDFT results for the deprotonated coumarins [**1-H**]$^-$ and [**5-H**]$^-$ correlate well with the experimental data (Fig. 9). Deprotonation of the parent coumarin **1** does not significantly change the composition of its HOMO and LUMO, but it does lead to a larger

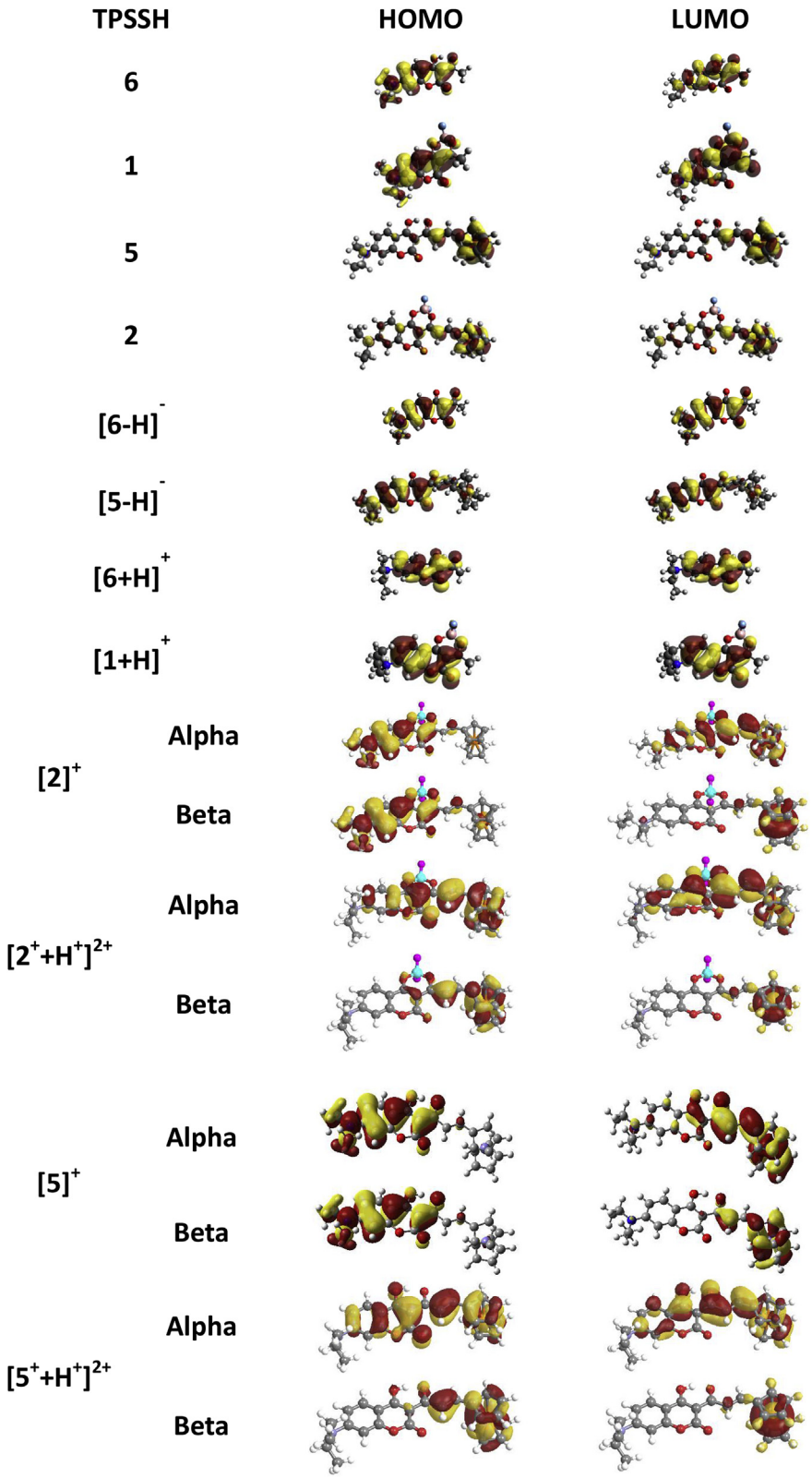

Fig. 8. DFT-predicted frontier MOs for the target coumarins.

HOMO-LUMO energy gap in [**1-H**]$^-$ (3.92 eV) compared to that in **1** (3.18 eV). The agreement with the measured shift to higher energy of the most intense $\pi \rightarrow \pi^*$ transition upon deprotonation indicates that it is dominated by the HOMO→LUMO single-electron excitation. TDDFT correctly predicted a ~50% loss in intensity compared to the parent coumarin **1** for the most intense band in [**1-H**]$^-$. TDDFT also explains transformation of the UV–vis spectrum for **5** upon deprotonation (Fig. 9). The deprotonation of **5** results in

Table 1
DFT-predicted molecular orbital compositions for the target coumarins.

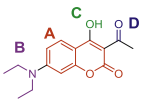

% Composition MO	E (eV)	A	B	C	D	E	F
73	**-5.462**	**48.0**	**47.0**	**0.9**	**4.1**		
74	***-2.282***	***57.0***	***10.1***	***9.0***	***23.9***		

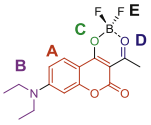

84	**-5.747**	**44.2**	**47.5**	**2.6**	**5.4**	**0.3**	
85	***-2.883***	***44.1***	***9.4***	***8.4***	***37.4***	***0.7***	

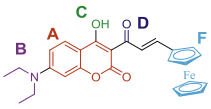

121	-5.415	45.2	44.3	0.9	4.1	5.5	
123	**-5.118**	**2.5**	**1.6**	**0.1**	**4**	**91.8**	
124	***-2.601***	***26.6***	***5.3***	***5.6***	***48.4***	***14.1***	

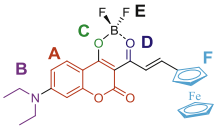

132	-5.616	38.8	40.9	1.7	5.1	0.2	13.3
134	**-5.295**	**5.9**	**3.7**	**0.1**	**4.1**	**0.0**	**86.2**
135	***-3.128***	***25.3***	***4.9***	***4.8***	***48.4***	***0.6***	***16.0***

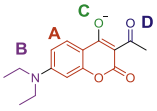

73	**-4.583**	**53.4**	**41.4**	**0.1**	**5.1**		
74	***-0.663***	***61.9***	***12.0***	***9.9***	***16.2***		

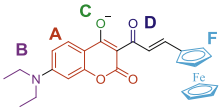

122	-4.693	6.6	4.6	2.2	7.7	78.9	
123	**-4.557**	**51.3**	**33.5**	**0.2**	**5.3**	**9.7**	
124	***-1.393***	***17.2***	***1.3***	***2.2***	***51.8***	***27.5***	
125	-0.504	48.1	8.2	4.8	6.2	32.7	

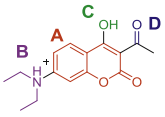

72	-7.551	28.6	0.0	10.3	61.1		
73	**-7.252**	**84.2**	**1.8**	**3.9**	**10.1**		
74	***-3.389***	***69.6***	***6.8***	***8.1***	***15.5***		

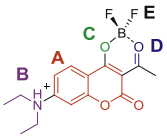

83	-7.991	76.0	1.8	7.8	11.4	3.0	
84	**-7.636**	**91.5**	**1.8**	**0.2**	**5.9**	**0.6**	
85	***-3.908***	***55.9***	***4.2***	***9.7***	***29.6***	***0.6***	

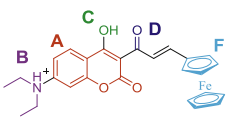

121	-6.044	0.3	0.0	0.1	3.5	96.1	

Table 1 (*continued*)

122	-5.431	0.0	0.0	0.0	0.3	99.7	
123	**-5.386**	**0.6**	**0.0**	**0.2**	**4.8**	**94.4**	
124	***-3.378***	***53.3***	***5.3***	***7.3***	***26.7***	***7.4***	
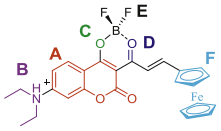							
132	-6.287	1.4	0.0	0.4	0.1	4.4	93.7
133	-5.728	0.0	0.0	0.0	0.0	0.2	99.8
134	**-5.669**	**1.9**	**0.1**	**0.6**	**0.1**	**5.5**	**91.8**
135	***-3.803***	***37.8***	***2.9***	***6.7***	***0.6***	***37.6***	***14.4***
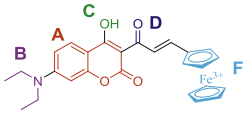							
α Set							
122	-6.848	94.0	4.6	0.2	1.1	0.1	
123	**-5.719**	**46.5**	**46.6**	**1.4**	**4.9**	**0.6**	
124	***-3.785***	***5.1***	***1.2***	***1.2***	***25.0***	***67.5***	
125	-3.369	0.1	0	0	0.4	99.5	
β set							
121	-6.846	93.9	4.6	0.2	1.1	0.1	
122	**-5.714**	**46.2**	**46.3**	**1.5**	**5.0**	**1.0**	
123	***-4.732***	***1.1***	***0.4***	***0.1***	***4.4***	***94.0***	
124	-3.349	11.5	2.6	2.6	39.9	43.4	
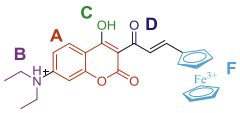							
α Set							
122	-7.951	53.3	1.2	0.3	25.9	19.3	
123	**-7.785**	**38.7**	**0.8**	**3.5**	**22.3**	**34.7**	
124	***-3.974***	***16.2***	***1.2***	***3.4***	***32.9***	***46.3***	
125	-3.428	0.3	0.0	0.0	0.6	99.1	
β set							
119	-8.125	14.8	0.3	1.0	25.0	58.9	
120	-7.886	77.6	1.8	2.6	7.9	10.0	
121	-7.71	0.1	0.0	0.0	0.2	99.7	
122	**-7.522**	**3.9**	**0.1**	**0.8**	**13.4**	**81.8**	
123	***-4.818***	***0.3***	***0.0***	***0.1***	***2.6***	***97.0***	
124	-3.771	32.0	2.6	5.7	39.0	20.7	
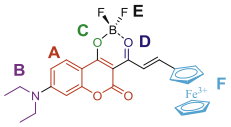							
α Set							
133	-7.48	94.5	3.1	0.0	0.0	1.6	0.9
134	**-6.303**	**44.7**	**44.5**	**2.6**	**0.3**	**6.2**	**1.7**
135	***-3.893***	***13.8***	***2.6***	***2.3***	***0.4***	***32.9***	***48.0***
β set							
130	-7.591	0.0	0.0	0.0	0.0	0.2	99.8
131	-7.485	92.8	2.1	0.2	0.1	1.3	3.5
132	-7.397	8.1	2.0	2.2	0.2	11.8	75.7
133	**-6.301**	**44.7**	**44.3**	**2.5**	**0.3**	**6.0**	**2.2**
134	***-4.702***	***0.7***	***0.2***	***0.1***	***0.0***	***2.6***	***96.4***
135	-3.647	19.9	3.7	3.5	0.5	44.6	27.8
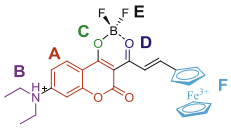							
α Set							
132	-8.668	45.2	1.4	1.4	1.7	14.4	35.9
133	-8.273	80.5	1.6	1.0	0.4	7.4	9.1
134	**-7.986**	**33.1**	**0.7**	**2.9**	**0.2**	**23.0**	**40.1**
135	***-4.472***	***22.3***	***1.3***	***5.4***	***0.5***	***42.2***	***28.3***
136	-3.555	2.6	0.2	0.3	0.0	1.3	95.6
β set							

(*continued on next page*)

Table 1 (*continued*)

130	-8.331	55.9	1.0	2.8	0.4	11.1	28.8
131	-8.158	58.5	1.3	0.9	0.2	8.6	30.5
132	-7.853	0.0	0.0	0.0	0.0	0.2	99.8
133	**-7.683**	**6.0**	**0.1**	**1.0**	**0.1**	**9.5**	**83.3**
134	***-4.977***	***1.5***	***0.1***	***0.4***	***0.1***	***5.2***	***92.7***
135	-4.308	27.9	1.8	6.2	0.5	42.9	20.7

* Bold lines are HOMO's
* Bold and italicized lines are LUMO's

significant destabilization of the coumarin-centered HOMO-2 orbital, which becomes the HOMO in [**5-H**]$^-$ (Table 1). In addition, deprotonation also leads to a larger HOMO-LUMO energy gap in [**5-H**]$^-$ compared to the neutral **5**. As a result, both MLCT and $\pi\rightarrow\pi^*$ transitions in [**5-H**]$^-$ have higher energy than similar bands in neutral **5**. This leads to the higher-energy shift of all bands in [**5-H**]$^-$ compared to coumarin **5**. TDDFT correctly predicts the ~50% drop in intensity for the most intense $\pi\rightarrow\pi^*$ transition upon deprotonation.

Protonation of the diethylamino group in parent coumarins **1** and **6** results in localization of the HOMO at the coumarin core, which leads to a loss of conjugation and a significant increase of the HOMO-LUMO energy gap in $[\mathbf{1}+\mathbf{H}]^+$ and $[\mathbf{6}+\mathbf{H}]^+$ compared to the respective neutral compounds (Table 1). TDDFT correctly predicts the lower-intensity and higher-energy shifts for the most intense coumarin-centered $\pi\rightarrow\pi^*$ transitions (Fig. 9). In the case of ferrocene-containing coumarin **5**, TDDFT predicts that the either protonation of the diethylamino group (formation of $[\mathbf{5}+\mathbf{H}]^+$) or oxidation of the ferrocene substituent (formation of $[\mathbf{5}]^+$) should result in the formation of an intense charge-transfer band at ~700 nm, which contradicts the experimental data. However, TDDFT-predicted UV–vis spectrum of both protonated and oxidized complex $[\mathbf{5}^+{+}\mathbf{H}^+]^{2+}$ would result in only low-intensity bands in the NIR region, and overall, the theoretical spectral profile fits well with the experimental data (Fig. 9). Similarly, TDDFT-predicted UV–vis spectra for either protonated $[\mathbf{2}+\mathbf{H}]^+$ or oxidized $[\mathbf{2}]^+$ coumarin are in disagreement with the experimentally observed overall higher-energy shift of the most intense transitions. However, TDDFT-predicted UV–vis spectrum of both protonated and oxidized $[\mathbf{2}^+{+}\mathbf{H}^+]^{2+}$ compound agree well with the experimental data (Fig. 9). It is also important to note that the TDDFT-predicted UV–vis spectrum of the oxidized $[\mathbf{2}]^+$ coumarin correlates well with the spectroelectrochemical data, providing us with more confidence that the acid titration data on interaction of the ferrocene-containing coumarines **2** and **5** (Fig. 2) reflects both protonation of the diethylamino group and oxidation of the ferrocene substituent by oxygen. Overall, DFT and TDDFT data explain well experimental and photophysical properties of the target coumarins and provide additional insights into their pH-dependent UV–vis spectra.

3. Conclusions

We have reported preparation and characterization of two fully conjugated ferrocene-containing coumarins **2** and **5** with and without the BF_2 chelating fragment. These new systems were characterized by a variety of spectroscopic, electrochemical and spectroelectrochemical methods. DFT calculations were indicative of the predominantly ferrocene-centered HOMO and coumarin-centered LUMO in coumarins **2** and **5**. TDDFT calculations correctly predicted the pH-dependence of the UV–vis spectra for all the coumarins presented. The photophysical properties of the target compounds were investigated by the steady-state fluorescence and ultrafast pump-probe spectroscopy. Selective photoexcitation of the coumarin core followed ultrafast electron transfer from the ferrocene fragment resulting in formation of a charge-separated Fc^+-$coumarin^{-\cdot}$ state. This charge-separated state undergoes ultrafast ground state recovery in 22–23 ps, which contrasts with the photophysical behavior of the coumarin precursors that have 1.3–1.5 ns excited state lifetimes. Support for ferrocene-facilitated formation of the charge-separated states was provided by steady-state fluorescence oxidative titrations, and DFT and TDDFT computational predictions.

4. Experimental section

4.1. General information

Reagents and materials. Solvents were purified using standard approaches: toluene was dried over sodium metal, DCM was dried over calcium hydride. Ferrocene carboxaldehyde, fullerene-[C_{60}], and sarcosine were purchased from Sigma Aldrich. Coumarin **1** was prepared as described earlier [24].

Spectroscopy Measurements. Jasco-720 spectrophotometer was used to collect UV–Vis data. Electrochemical cyclic voltammetry (CV) and differential pulse voltammetry (DPV) measurements were conducted using a CH Instruments electrochemical analyzer utilizing a three-electrode scheme with platinum working, auxiliary and Ag/AgCl reference electrodes. DCM was used as solvents and 0.1 M solution of tetrabutylammonium perchlorate (TBAP) was used as supporting electrolyte. In all cases, experimental redox potentials were corrected using decamethylferrocene (Fc*H) as an internal standard. NMR spectra were recorded on a Bruker Avance instrument with a 300 MHz frequency for protons and 75 MHz frequency for carbons. Chemical shifts are reported in parts per million (ppm) and referenced to tetramethylsilane ($Si(CH_3)_4$) as an internal standard. High-resolution mass spectra of compounds **3, 4,** and **5** were recorded using a Bruker micrOTOF-QIII.

Computational Details. The starting geometry of compounds **3, 5** were optimized using a TPSSh exchange-correlation functional [56]. Energy minima in optimized geometry was confirmed by the frequency calculations (absence of the imaginary frequencies). Solvent effect was calculated using the polarized continuum model (PCM) [57]. In all calculations, DCM was used as the solvent. In PCM-TDDFT calculation, the first 50 states were calculated. Full-electron Wachter's basis set [58] was utilized for iron atoms, while all other atoms were modeled using 6-31G(d) [59] basis set. Gaussian 09 software was used in all calculations [60]. QMForge program was used for molecular orbital analysis [61].

Pump-probe spectroscopy. A home-built laser system consisting of a Ti:sapphire oscillator (powered by a Spectra Physics Millenia Pro) and regenerative amplifier (powered by a Spectra Physics Empower 15 or Evolution) generated ~60 to 80 fs (FWHM), 0.8–1.0 mJ, **810** nm pulses at a repetition rate of 1 kHz. A portion of this light was directed into a home-built noncollinear optical parametric amplifier (NOPA) to create excitation pulses at **530** nm, **570** nm and **650** nm. Continuum probe pulses of **420**–**750** nm, and **850**–**1400** nm, were created by focusing a small fraction of the **805** nm–**815** nm light (~20 μW) into a 2 mm sapphire window and

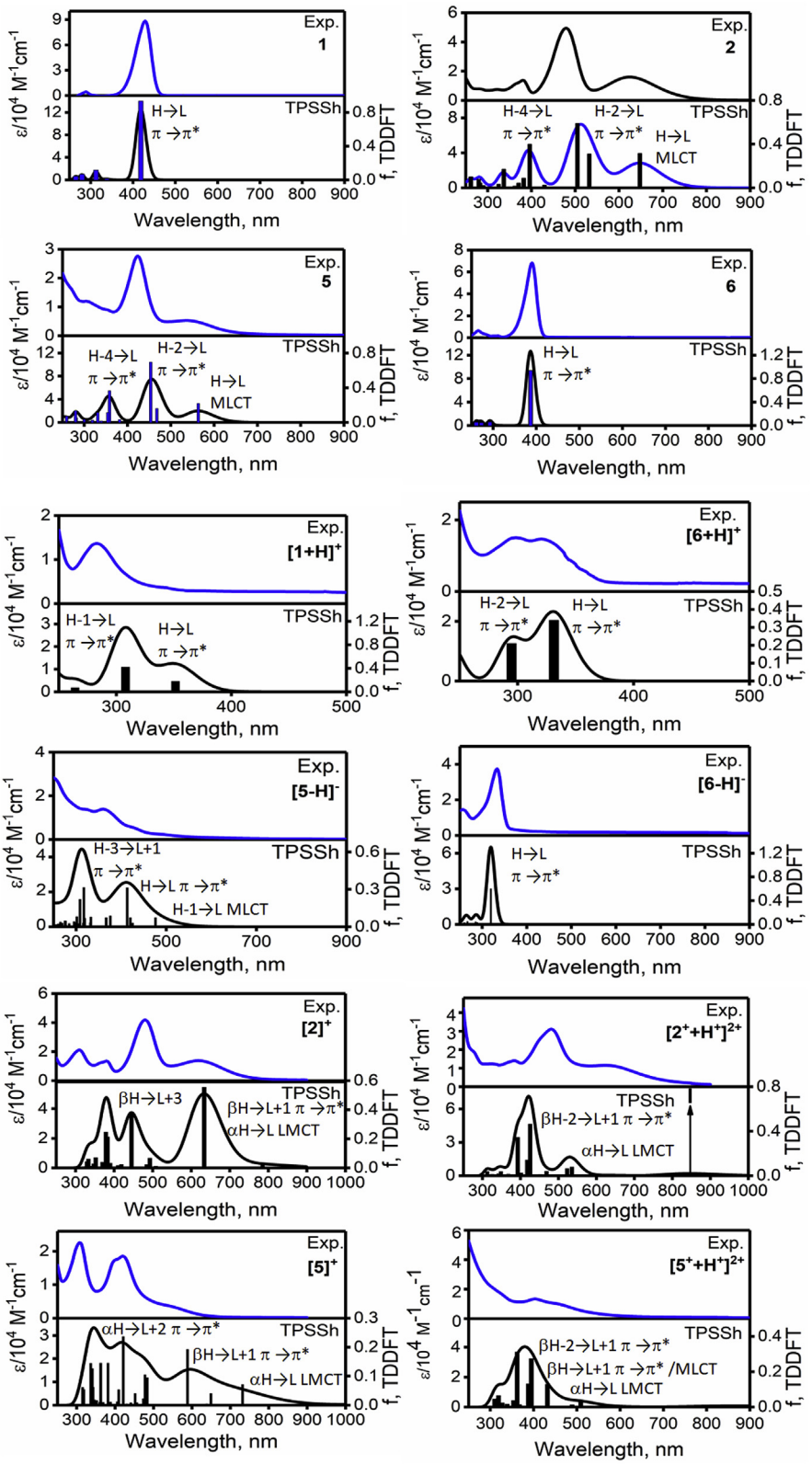

Fig. 9. Experimental (top) and TDDFT-predicted (bottom) UV–vis spectra of the target coumarins. Predominant single-electron excitations and the nature of excited states for the key TDDFT-predicted transitions are listed above each spectrum.

Yttrium Aluminum Garnet (YAG) crystal, respectively. The excitation light was polarized at 54.7° relative to the probe polarization (the magic angle) to isolate the isotropic dynamics of the excited state. Time delay between the excitation and probe pulses was controlled by a mechanical delay stage (Newport UTM150PP.1). Pump and probe pulses were focused and spatially overlapped in 1 mm quartz cuvette containing the sample. The probe beam emerging from the sample was collimated, directed through a monochromator and detected on an array. A Princeton Instruments SP2150i monochromator (150 lines/mm, 500 nm blaze) with an attached 256 pixel diode array (Hamamatsu S3902-256Q) was used for visible light. A Princeton Instruments SP2150 monochrometer (150 lines/mm, 1200 nm blaze) with an attached 256 linear pixel InGaAs diode array (Hamamatsu G9213-256S) was used for infrared light. The pump beam was chopped at half the laser repetition rate while each laser pulse of the probe beam was measured to yield the change in optical density, ΔOD. The ΔOD was determined for each pulse pair. Typically, 20,000–40,000 pulse pairs were averaged for each time point presented in the pump-probe data. Data shown was collected with pump energies typically between 60 nJ and 150 nJ per pulse. Samples had an optical density of 0.25–0.35 at the excitation wavelength. Absorption spectra taken before and after the pump probe experiments were indistinguishable, indicating no evidence of sample degradation.

4.2. Synthesis

Compound 2: To the mixture of coumarin **1** (200 mg, 0.619 mmol) and ferrocenecarboxaldehyde (159 mg, 0.74 mmol) in dry toluene (15 mL) the mixture of piperidine (263 mg, 3.09 mmol) and acetic acid (520 mg, 8.66 mmol) was added. The resulting solution was heated under reflux for 20 min. Then the solution was cooled down to room temperature, evaporated, washed with water, filtered and air dried. The crude product was stirred in cold methanol for 30 min and filtered to give 300 mg (93%) of pure dyad **2.** ^{1}H NMR (500 MHz, $CDCl_3$) δ 8.45 (d, $^{3}J_{H,H} = 15.0$ Hz, 1H), 8.00–7.96 (m, 2H), 6.66 (dd, $^{3}J_{H,H} = 9.0$ Hz, $^{4}J_{H,H} = 2.5$ Hz, 1H), 6.38 (d, $^{4}J_{H,H} = 2.5$ Hz, 1H), 4.79 (s, 4H), 4.27 (s, 5H), 3.52 (q, $^{3}J_{H,H} = 7.0$ Hz, 2H), 1.27 (t, $^{3}J_{H,H} = 7.0$ Hz, 3H); ^{13}C NMR (125 MHz, $CDCl_3$) δ 159.54, 158.40, 156.87, 155.25, 128.66, 116.09, 109.97, 96.38, 79.15, 74.47, 70.98, 70.89, 45.41, 12.41; HRMS (APCI negative) calcd for $C_{26}H_{24}BF_2NO_4$ [M]: 519.1115, found 519.1202.

Compound 3: The mixture of compound **2** (150 mg, 0.29 mmol) and aluminum chloride (115 mg, 0.86 mmol) in dry DCM was refluxed for 3 min and then treated with the solution of 3,4-dihydroxybenzaldehyde (200 mg, 1.45 mmol). The resulting mixture was stirred for 2 h at room temperature. Then the insoluble particles were filtered off and the resulting DCM solution was washed with water (2 × 50 mL), the organic layer was dried (Na_2SO_4) and evaporated to dryness. The crude product was purified by column chromatography on silica gel using hexane –ethyl acetate (1:1) system to give 72 mg (40%) of dyad **3**. ^{1}H NMR (500 MHz, $CDCl_3$) δ 10.33 (s, 1H), 8.41 (d, $^{3}J_{H,H} = 15.0$ Hz, 1H), 8.05 (d, $^{3}J_{H,H} = 15.0$ Hz, 1H), 7.92 (d, $^{3}J_{H,H} = 7.6$ Hz, 1H), 7.26 (s, 1H), 7.03 (s, 1H), 6.87 (s, 1H), 6.61 (d, $^{3}J_{H,H} = 7.6$ Hz, 1H), 6.39 (s, 1H), 4.80–4.78 (m, 4H), 4.26 (s, 5H), 3.49–3.47 (m, 4H), 1.27–1.24 (m, 6H); HRMS (APCI positive) calcd for $C_{33}H_{28}BFeNO_7$ [M+H]: 618.1381, found 618.1406.

Compound 5: The mixture of compound **3** (130 mg, 0.21 mmol), fullerene-C_{60}(302 mg, 0.42 mmol), and sarcosine (2.1 mmol, 187 mg) was refluxed in dry toluene (40 mL) for 2h. Then the solution was cooled down to room temperature, the unreacted fullerene and sarcosine were filtered off, and the toluene solution was evaporated to dryness. The crude product was purified by column chromatography on silica gel using toluene as a solvent to give 49 mg (50%) of compound **5.** ^{1}H NMR (500 MHz, $CDCl_3$) δ 8.10 (s, 1H), 8.03–7.95 (m, 2H), 7.85 (m, 1H), 6.60 (m, 1H), 6.37 (s, 1H), 4.68 (s, 2H), 4.54 (s, 2H), 4.20 (s, 5H), 3.47 (m, 4H), 1.27 (m, 6H); ^{13}C NMR (125 MHz, $CDCl_3$) δ 161.62, 157.31, 153.77, 148.66, 129.59, 127.28, 120.10, 108.97, 96.49, 79.68, 72.21, 70.19, 45.18, 12.63; HRMS (APCI negative) calcd for $C_{26}H_{24}NO_4$ [M]: 470.1061, found 470.1143.

Acknowledgment

Generous support from the Minnesota Supercomputing Institute, NSERC, CFI, NSF (CHE-1464711 and MRI-1420373) University of Manitoba, and WestGrid Canada to VN is greatly appreciated. Generous support from the NSF (DMR-1708177) to DAB is greatly appreciated.

Appendix A. Supplementary data

Supplementary data to this article can be found online at https://doi.org/10.1016/j.jorganchem.2019.03.004.

References

[1] J. Li, C. Yin, F. Huo, Development of fluorescent zinc chemosensors based on various fluorophores and their applications in zinc recognition, Dyes Pigments 131 (2016) 100–133.
[2] B. Kalyanaraman, M. Hardy, J. Zielonka, A critical review of methodologies to detect reactive oxygen and nitrogen species stimulated by NADPH oxidase enzymes: implications in pesticide toxicity, Curr. Pharm. Reports 2 (2016) 193–201.
[3] J. He, F. Yan, D. Kong, Q. Ye, X. Zhou, L. Chen, Fluorescent probes for glutathione detection quick view other sources, Curr. Org. Chem. 20 (2016) 2718–2734.
[4] V.F. Traven, A.V. Manaev, A.Yu Bochkov, T.A. Chibisova, I.V. Ivanov, New reactions, functional compounds, and materials in the series of coumarin and its analogs, Russ. Chem. Bull. 61 (2012) 1342–1362.
[5] Y. Jeong, J. Yoon, Recent progress on fluorescent chemosensors for metal ions, Inorg. Chim. Acta 381 (2012) 2–14.
[6] Y. Song, Z. Chen, H. Li, Advances in coumarin-derived fluorescent chemosensors for metal ions, Curr. Org. Chem. 16 (2012) 2690–2707.
[7] S.T. Manjare, Y. Kim, D.G. Churchill, Selenium- and tellurium-containing fluorescent molecular probes for the detection of biologically important analytes, Acc. Chem. Res. 47 (2014) 2985–2998.
[8] V.F. Traven, A.Y. Bochkov, Synthesis and photochromism of aryl(heteroaryl)- and diheteroarylethenes-coumarin derivatives, Heterocycl. Commun. 19 (2013) 219–238.
[9] M. Rajeshirke, M.C. Sreenath, S. Chitrambalam, I.H. Joe, N. Sekar, Enhancement of NLO properties in OBO fluorophores derived from carbazole-coumarin chalcones containing carboxylic acid at the N- alykl terminal end, J. Phys. Chem. C 122 (2018) 14313–14325.
[10] M. Waheed, N. Ahmed, M.A. Alsharif, M.I. Alahmdi, S. Mukhtar, One-pot synthesis of 1,5-diketones from 3-acetyl-4-hydroxycoumarin and effective cyclization to unexpected 3,4-dihydropyridines, Org. Biomol. Chem. 16 (2018) 3428–3437.
[11] A. Bonardi, M. Falsini, D. Catarzi, F. Varano, L. Di Cesare Mannelli, B. Tenci, C. Ghelardini, A. Angeli, C.T. Supuran, V. Colotta, Structural investigations on coumarins leading to chromeno[4,3-c]pyrazol-4-ones and pyrano[4,3-c]pyrazol-4-ones: new scaffolds for the design of the tumor-associated carbonic anhydrase isoforms IX and XII, Eur. J. Med. Chem. 146 (2018) 47–59.
[12] O. Guzman-Mendez, F. Gonzalez, S. Bernes, M. Flores-Alamo, J. Ordonez-Hernandez, H. Garcia-Ortega, J. Guerrero, W. Qian, N. Aliaga-Alcalde, L. Gasque, Coumarin derivative directly coordinated to lanthanides acts as an excellent antenna for UV-Vis and Near-IR emission, Inorg. Chem. 57 (2018) 908–911.
[13] D.Lj Stojkovic, V.V. Jevtic, N. Vukovic, M. Vukic, P. Canovic, M.M. Zaric, M.M. Misic, D.M. Radovanovic, D. Baskic, S.R. Trifunovic, Synthesis, characterization, antimicrobial and antitumor reactivity of new palladium(II) complexes with methionine and tryptophane coumarine derivatives, J. Mol. Struct. 1157 (2018) 425–433.
[14] V. Stefanou, D. Matiadis, D. Tsironis, O. Igglessi-Markopoulou, V. McKee, J. Markopoulos, Synthesis and single crystal X-ray diffraction studies of coumarin-based Zn(II) and Mn(II) complexes, involving supramolecular interactions, Polyhedron 141 (2018) 289–295.
[15] L.N. Sharada, M.C. Ganorkar, Complexes of oxovanadium(IV), chromium(III), manganese(II), iron(II), cobalt(II), nickel(II) and copper(II) with 6-chloro-4-hydroxy-3-acetylcoumarin (Cl-HAC), Indian J. Chem., Sect. A: Inorg. Phys. Theor. Anal. 27A (1988) 542–544.
[16] V.K. Rastogi, J.P. Goel, B.S. Tyagi, R.C. Saxena, R.K. Kela, Synthesis and spectral studies on complexes of p-(dimethylamino)anil of 3-acetyl-4-

hydroxycoumarin glyoxal with platinum(4+), iridium(3+) and uranyl(2+) metal ions, J. Indian Chem. Soc. 60 (1983) 783–786.
[17] H.D. Ilge, D. Fassler, H. Hartmann, Spectroscopy, photochemistry, and photophysics of boron chelates. 1. Absorption and fluorescence behavior of substituted 1,3-diketoborates, Z. Chem. 24 (1984) 218–219.
[18] Y. Erande, S. Kothavale, M.C. Sreenath, S. Chitrambalam, I.H. Joe, N. Sekar, Triphenylamine derived coumarin chalcones and their red emitting OBO difluoride complexes: synthesis, photophysical and NLO property study, Dyes Pigments 148 (2018) 474–491.
[19] A.B. Tathe, N. Sekar, Red-emitting NLOphoric carbazole-coumarin hybrids - synthesis, photophysical properties and DFT studies, Dyes Pigments 129 (2016) 174–185.
[20] I.A. Karpenko, Y. Niko, V.P. Yakubovskyi, A.O. Gerasov, D. Bonnet, Y.P. Kovtun, A.S. Klymchenko, Push-pull dioxaborine as fluorescent molecular rotor: far-red fluorogenic probe for ligand-receptor interactions, J. Mater. Chem. C: Mater. Optic. Electron. Dev. 4 (2016) 3002–3009.
[21] A.V. Nyuchev, K.V. Schegravin, M.A. Lopatin, V.V. Fokin, I.P. Beletskaya, A.Yu Fedorov, Synthesis of fluorescent boron difluoride complexes of 3-acyl-4-hydroxycoumarins, Synthesis 46 (2014) 3239–3248.
[22] A.O. Gerasov, K.V. Zyabrev, M.P. Shandura, Y.P. Kovtun, The structural criteria of hydrolytic stability in series of dioxaborine polymethine dyes, Dyes Pigments 89 (2011) 76–85.
[23] L.A. Padilha, S. Webster, O.V. Przhonska, H. Hu, D. Peceli, T.R. Ensley, M.V. Bondar, A.O. Gerasov, Y.P. Kovtun, M.P. Shandura, Efficient Two-Photon absorbing Acceptor-π-Acceptor polymethine dyes, J. Phys. Chem. A 114 (2010) 6493–6501.
[24] A.O. Gerasov, M.P. Shandura, YuP. Kovtun, Series of polymethine dyes derived from 2,2-difluoro-1,3,2-(2H)-dioxaborine of 3-acetyl-7-diethylamino-4-hydroxycoumarin, Dyes Pigments 77 (2008) 598–607.
[25] S. Sundharamurthi, K. Sudha, S. Karthikaikumar, K. Abinaya, V.R. Reddy, P. Kalimuthu, Switching of inter-valence charge transfer in stimuli-responsive bis(ferrocenyl)porphyrin, New J. Chem. 42 (2018) 4742–4747.
[26] N.R. Erickson, C.D. Holstrom, H.M. Rhoda, G.T. Rohde, Y.V. Zatsikha, P. Galloni, V.N. Nemykin, Tuning Electron-Transfer properties in 5,10,15,20-tetra(1'-hexanoylferrocenyl)porphyrins as prospective systems for quantum cellular automata and platforms for Four-Bit information storage, Inorg. Chem. 56 (2017) 4717–4728.
[27] S.J. Dammer, P.V. Solntsev, J.R. Sabin, V.N. Nemykin, Synthesis, characterization, and Electron-Transfer processes in indium Ferrocenyl-Containing porphyrins and their fullerene adducts, Inorg. Chem. 52 (2013) 9496–9510.
[28] J. Rochford, A.D. Rooney, M.T. Pryce, Redox control of meso-Zinc(II) ferrocenylporphyrin based fluorescence switches, Inorg. Chem. 46 (2007) 7247–7249.
[29] A.I. Arkhypchuk, A. Orthaber, K.E. Borbas, Synthesis and characterization of ferrocenyl chlorins, 1,1'-Ferrocene-Linked chlorin dimers, and their BODIPY analogues, Inorg. Chem. 56 (2017) 3044–3054.
[30] W.-J. Shi, P.-C. Lo, S. Zhao, R.C.H. Wong, Q. Wang, W.-P. Fong, D.K.P. Ng, A biotin-conjugated glutathione-responsive FRET-based fluorescent probe with a ferrocenyl BODIPY as the dark quencher, Dalton Trans. 45 (2016) 17798–17806.
[31] Y.V. Zatsikha, N.O. Didukh, T. Blesener, M.P. Kayser, Y.P. Kovtun, D.A. Blank, V.N. Nemykin, Preparation, characterization, redox, and photoinduced Electron-Transfer properties of the NIR-Absorbing N-Ferrocenyl-2-Pyridone BODIPYs, Eur. J. Inorg. Chem. (2017) 318–324.
[32] Y.V. Zatsikha, E. Maligaspe, A.A. Purchel, N.O. Didukh, Y. Wang, Y.P. Kovtun, D.A. Blank, V.N. Nemykin, Tuning electronic structure, redox, and photophysical properties in asymmetric NIR-Absorbing organometallic BODIPYs, Inorg. Chem. 54 (2015) 7915–7928.
[33] R. Misra, B. Dhokale, T. Jadhav, S.M. Mobin, Heteroatom-connected ferrocenyl BODIPYs: synthesis, structure, and properties, Organometallics 33 (2014) 1867–1877.
[34] R. Misra, B. Dhokale, T. Jadhav, S.M. Mobin, Donor-acceptor meso-alkynylated ferrocenyl BODIPYs: synthesis, structure, and properties, Dalton Trans. 42 (2013) 13658–13666.
[35] O. Galangau, I. Fabre-Francke, S. Munteanu, C. Dumas-Verdes, G. Clavier, R. Meallet-Renault, R.B. Pansu, F. Hartl, F. Miomandre, Electrochromic and electrofluorochromic properties of a new boron dipyrromethene-ferrocene conjugate, Electrochim. Acta 87 (2013) 809–815.
[36] E. Maligaspe, T.J. Pundsack, L.M. Albert, Y.V. Zatsikha, P.V. Solntsev, D.A. Blank, V.N. Nemykin, Synthesis and Charge-Transfer dynamics in a Ferrocene-Containing organoboryl aza-BODIPY Donor-Acceptor triad with boron as the hub, Inorg. Chem. 54 (2015) 4167–4174.
[37] R. Sharma, R. Maragani, R. Misra, Ferrocenyl aza-dipyrromethene and aza-BODIPY: synthesis and properties, J. Organomet. Chem. 825–826 (2016) 8–14.
[38] Y.V. Zatsikha, D.B. Nemez, R.L. Davis, S. Singh, D.E. Herbert, A.J. King, C.J. Ziegler, V.N. Nemykin, Testing the limits of the BOPHY platform: preparation, characterization, and theoretical modeling of BOPHYs and organometallic BOPHYs with Electron-Withdrawing groups at β-Pyrrolic and bridging positions, Chem. Eur J. 23 (2017) 14786–14796.
[39] H.M. Rhoda, K. Chanawanno, A.J. King, Y.V. Zatsikha, C.J. Ziegler, V.N. Nemykin, Unusually strong Long-Distance Metal-Metal coupling in bis(ferrocene)-containing BOPHY: an introduction to organometallic BOPHYs, Chem. Eur J. 21 (2015) 18043–18046.
[40] J. Qu, Q. Xia, W. Ji, S. Jing, D. Zhu, L. Li, L. Huang, Z. An, C. Xin, Y. Ni, A ferrocene∩europium assembly showing phototriggered anticancer activity and fluorescent modality imaging, Dalton Trans. 47 (2018) 1479–1487.
[41] B. Li, Q. Liu, Y. Zhou, Z. Jia, M. Zhu, Y. Xu, M. Song, Synthesis and properties of 4-ferrocenyl-carboxybenzene-coumarin derivatives, You Ji Hua Xue 37 (2017) 2008–2014.
[42] S.R. Bhatta, V. Bheemireddy, A. Thakur, A redox-driven fluorescence "off-on" molecular switch based on a 1,1'-unsymmetrically substituted ferrocenyl coumarin system: mimicking combinational logic operation, Organometallics 36 (2017) 829–838.
[43] S. Kumar, A. Patel, N. Ahmed, Microwave-assisted expeditious and efficient synthesis of novel quinolin-4-ylmethoxychromen-2- and -4-ones catalyzed by YbCl3 under a solvent-free one-pot three component domino reaction and their antimicrobial activity, RSC Adv. 5 (2015) 93067–93080.
[44] J. Yu, L.-L. Gao, P. Huang, D.-L. Wang, Crystal structure of 4-methyl-2-oxo-2H-chromen-7-yl ferrocenecarboxylate, Acta Cryst, Section E: Struct. Rep. Online 70 (2014) m369–m370.
[45] G.K. Verma, R.K. Verma, M.S. Singh, Construction of five- and six-membered heterocycles on both Cp rings of the ferrocene moiety of α-oxoketene-S,S-acetal and β-oxodithioester via heteroaromatic annulation, RSC Adv. 3 (2013) 245–252.
[46] I. Arellano, P. Sharma, L. Rubio-Perez, A. Cabrera, N. Rosas, A. Toscano, Synthesis of new 7-ferrocenyl-β-enaminone-coumarins and ferrocenyl-pyrano [3,2-g]quinolin-2-ones from coumarin and ferrocenyl-α-ketoalkynes using Ni(CN)2/NaOH/H2O/CO/KCN aqueous catalytic system, J. Organomet. Chem. 700 (2012) 29–35.
[47] W.-F. Wang, J. Fan, C.-Z. Luo, Y.-F. Yuan, Y.-F. Zhang, A Synthesis of Ferrocenyl Dihydrocoumarin and Ferrocenyl dihydroquinolin-2(1H) - ones, ARKIVOC xi, 2011, pp. 105–120.
[48] M. Camur, A.A. Esenpinar, A.R. Ozkaya, M. Bulut, Synthesis, characterization, spectroscopic and electrochemical properties of phthalocyanines substituted with four 3-ferrocenyl-7-oxycoumarin moieties, J. Organomet. Chem. 696 (2011) 1868–1873.
[49] M. Maggini, G. Scorrano, M. Prato, Addition of azomethine ylides to C60: synthesis, characterization, and functionalization of fullerene pyrrolidines, J. Am. Chem. Soc. 115 (1993) 9798–9799.
[50] V. Georgakilas, K. Kordatos, M. Prato, D.M. Guldi, M. Holzinger, A. Hirsch organic functionalization of carbon nanotubes, J. Am. Chem. Soc. 124 (2002) 760–761.
[51] J. Lubach, W. Drenth, Enolization and oxidation. II. Oxidation of ferrocene by molecular oxygen and hydrogen peroxide in acidic media, Recl. Trav. Chim. Pays-Bas 92 (1973) 586–592.
[52] V.I. Ignatov, V.T. Solomatin, A.A. Nemodruk, Electrochemical properties of the ferrocene-ferricenium system in acidic organo-aqueous media, Zh. Anal. Khim. 33 (1978) 1268–1273.
[53] V.N. Nemykin, T.S. Blesener, C.J. Ziegler Photophysics, Redox processes, and electronic structures of ferrocenyl-containing BODIPYs, aza-BODIPYs, BOPHYs, transition-metal dipyrromethenes and aza-dipyrromethenes, Macroheterocycles 10 (2017) 9–26, https://doi.org/10.6060/mhc170188n.
[54] A. Samanta, R.W. Fessenden, Excited-state dipole moment of 7-amino-coumarins as determined from time-resolved microwave dielectric absorption measurements, J. Phys. Chem. A 104 (2000) 8577–8582.
[55] S.I. Druzhinin, B.D. Bursulaya, B.M. Uzhinov, Planar and twisted intramolecular charge transfer states of the excited proton transfer products of aminocoumarins, J. Photochem. Photobiol. A Chem. 90 (1995) 53–56.
[56] J.M. Tao, J.P. Perdew, V.N. Staroverov, G.E. Scuseria, Climbing the density functional ladder: nonempirical meta-generalized gradient approximation designed for molecules and solids, Phys. Rev. Lett. 91 (2003) 146401.
[57] J. Tomasi, B. Mennucci, R. Cammi, Quantum mechanical continuum solvation models, Chem. Rev. 105 (2005) 2999–3093.
[58] A.J.H. Wachters, Gaussian basis set for molecular wavefunctions containing third-row atoms, J. Chem. Phys. 52 (1970) 1033–1036.
[59] W.J. Hehre, R. Ditchfield, J.A. Pople, Self-Consistent Molecular Orbital Methods. 12. Further extensions of Gaussian-type basis sets for use in molecular-orbital studies of organic-molecules, J. Chem. Phys. 56 (1972) 2257.
[60] M.J. Frisch, G.W. Trucks, H.B. Schlegel, G.E. Scuseria, M.A. Robb, J.R. Cheeseman, G. Scalmani, V. Barone, B. Mennucci, G.A. Petersson, H. Nakatsuji, M. Caricato, X. Li, H.P. Hratchian, A.F. Izmaylov, J. Bloino, G. Zheng, J. L Sonnenberg, M. Hada, M. Ehara, K. Toyota, R. Fukuda, J. Hasegawa, M. Ishida, T. Nakajima, Y. Honda, O. Kitao, H. Nakai, T. Vreven, J.A. Montgomery Jr., J.E. Peralta, F. Ogliaro, M. Bearpark, J.J. Heyd, E. Brothers, K.N. Kudin, V.N. Staroverov, R. Kobayashi, J. Normand, K. Raghavachari, A. Rendell, J.C. Burant, S.S. Iyengar, J. Tomasi, M. Cossi, N. Rega, N.J. Millam, M. Klene, J.E. Knox, J.B. Cross, V. Bakken, C. Adamo, J. Jaramillo, R. Gomperts, R.E. Stratmann, O. Yazyev, A.J. Austin, R. Cammi, C. Pomelli, J.W. Ochterski, R.L. Martin, K. Morokuma, V.G. Zakrzewski, G.A. Voth, P. Salvador, J.J. Dannenberg, S. Dapprich, A.D. Daniels, O. Farkas, J.B. Foresman, J.V. Ortiz, J. Cioslowski, D.J. Fox, Gaussian 09, Revision D.1, Gaussian, Inc., Wallingford, CT, 2009.
[61] A.L. Tenderholt, QMForge, Version 2.1. Stanford University, Stanford, CA, USA. http://qmforge.sourceforge.net/.